

## Fatigue Behavior of Additive Manufactured 304L Stainless Steel Including Surface Roughness Effects

Seungjong Lee<sup>1,2</sup>, Jonathan Pegues<sup>1,2</sup>, Nima Shamsaei<sup>1,2\*</sup>

<sup>1</sup> Department of Mechanical Engineering, Auburn University, Auburn, AL 36849, USA

<sup>2</sup> National Center for Additive Manufacturing Excellence (NCAME), Auburn University,  
Auburn, AL 36849, USA

\*Corresponding Author: [shamsaei@auburn.edu](mailto:shamsaei@auburn.edu)

### Abstract

The fatigue behavior of additive manufactured parts in the as-built surface condition is typically dominated by the surface roughness. However, the fatigue behavior of 304L stainless steel fabricated by laser beam powder bed fusion shows less sensitivity to surface roughness under strain-controlled loading conditions than other additive manufactured materials. Under force-controlled conditions, however, the high cycle fatigue resistance is much lower for the as-built surface condition than the machined one. This study investigates the underlying mechanisms responsible for fatigue failure for each condition (i.e. strain-controlled or force-controlled). The corresponding cyclic deformation behavior was characterized, and a thorough fractography analysis was performed to identify the features responsible for crack initiation. Results indicate that the crack initiation features in both loading conditions are similar, and that the reduced high cycle fatigue resistance for force-controlled fatigue loading compared to strain-controlled one is related to differences in the cyclic deformation behavior of the material.

**Keywords:** Additive manufacturing; Laser beam powder bed fusion (LB-PBF); Surface roughness; Stainless steel; Fatigue;

### Introduction

Metal additive manufacturing (AM) is a popular technology in high tech industries such as biomedical and aerospace. Even though AM was introduced decades ago, its progress has been lagging due to the lack of advancements in other related technologies such as laser technology and computer aided design (CAD) [1]. It was only recently that AM has expanded, and metal AM in specific has emerged with several methods: laser beam powder bed fusion (LB-PBF), electron beam powder bed fusion (EB-PBF), and laser beam directed energy deposition (LB-DED) as viable manufacturing techniques [2]. The basic principle of AM is building the component layer-by-layer, thus AM can build complex geometries without the need for assembling multiple components. For the biomedical industry, AM can not only provide implants tailored to an individual patient and a specific injury but also reduce the stiffness of the implants to be more comparable to cortical bones. In the aerospace industry, AM enables light-weighting to improve

fuel-efficiency, using lattice structure or topology optimization. As a result, AM is recognized as an innovative manufacturing technique offering significant advantages over more traditional manufacturing methods.

LB-PBF is one of the most common metal AM methods, and its fabricated components have the most competitive mechanical properties among other AM methods [3]. Complex geometries and orientations can be sufficiently supported; hence the chance of collapse is lower than other AM techniques such as DED. In addition, the typical layer thickness of LB-PBF can be as low as 20  $\mu\text{m}$ , offering the best surface finish among the various metal AM techniques [4]. However, despite the improved surface finish of LB-PBF materials, the fatigue behavior of as-built parts is still dominated by the surface roughness [5]. Therefore, LB-PBF is studied as a state-of-the-art AM technology especially for fatigue critical applications.

Additively manufactured parts have comparable or even better strengths under static loading but often suffer from low or poor ductility. Additionally, under cyclic loading, most AM materials show insufficient performance compared to their wrought counterparts [6], [7], [8]. It has been estimated that more than half of the mechanical failures and fractures are caused by fatigue [9], thus many studies have investigated the fatigue behavior of additive manufactured materials [10], [11]. Yet the underlying effects of the AM process on the resulting structure of the material and their eventual fatigue resistance is not fully established [9], [11], [12]. As such, the adoption of AM across many industries has been limited by their reliability concerns under fatigue loading. Moreover, fatigue behavior is primarily influenced by defects at or near the surface which can initiate and grow cracks leading to premature part failure. It is further impacted by coarse surface roughness that can behave as micro-notches and induce fatigue cracks in the early stages of fatigue life. As a result, the fatigue behavior of AM parts is dependent by surface roughness.

304L SS is one of the most common austenitic stainless steels and it has many advantages such as corrosion resistance and a remarkable combination of strength and ductility [9], [12]. Because of these advantages, 304L SS is used in various fields such as nuclear, aeronautical, automotive, and marine industries. Therefore, LB-PBF AM 304L SS can create a synergy effect from the material itself and its ease of fabrication through AM techniques. However, there is limited information regarding LB-PBF 304L stainless steel (SS), especially in regards to its fatigue behavior. This paper investigates the influence of surface roughness on LB-PBF AM 304L SS under force-controlled and strain-controlled conditions. The fatigue behavior for both as-built and as-machined specimens are presented to understand the effects of surface roughness on the resulting fatigue performance.

### **Experimental Procedure**

The fabrication was conducted using an EOS M290 (EOS, Krailling, Germany) LB-PBF AM machine, and 304L SS powder from LPW Technology Inc. (LPW, Runcorn, UK) with a

reported particle size between 15-45  $\mu\text{m}$ . The EOS M290 was operated with default parameters from EOS itself: laser power of 195 W, the scan speed of 1083 mm/s, the hatching distance of 90  $\mu\text{m}$ , and the layer thickness of 20  $\mu\text{m}$ . Two different geometries were fabricated in the vertical direction including square machining blanks and net-shaped fatigue specimens [13].

The surface roughness of the as-built specimen gage sections was investigated using a Keyence VHX-6000 digital microscope (Keyence, Osaka, Japan). The direction of measurement was parallel to both build orientation and load direction. According to the specimen identification number on the top of specimens, the surfaces of the north, west, south, and east sides were measured longitudinally. The movement of the recoater arm, in relation to the specimen, is from east to west (from the feedstock bin to the overflow bin) and the direction of gas flow is from north to south (from the back part of the machine to the front) for all specimens. Line surface roughness measurements at 1000x magnification of microscope were taken approximately 2 mm in length along the build direction a minimum of three times and averaged. Figure 1 details the build orientation, the profiled area for line roughness measurement, and the direction of recoater arm and gas flow.

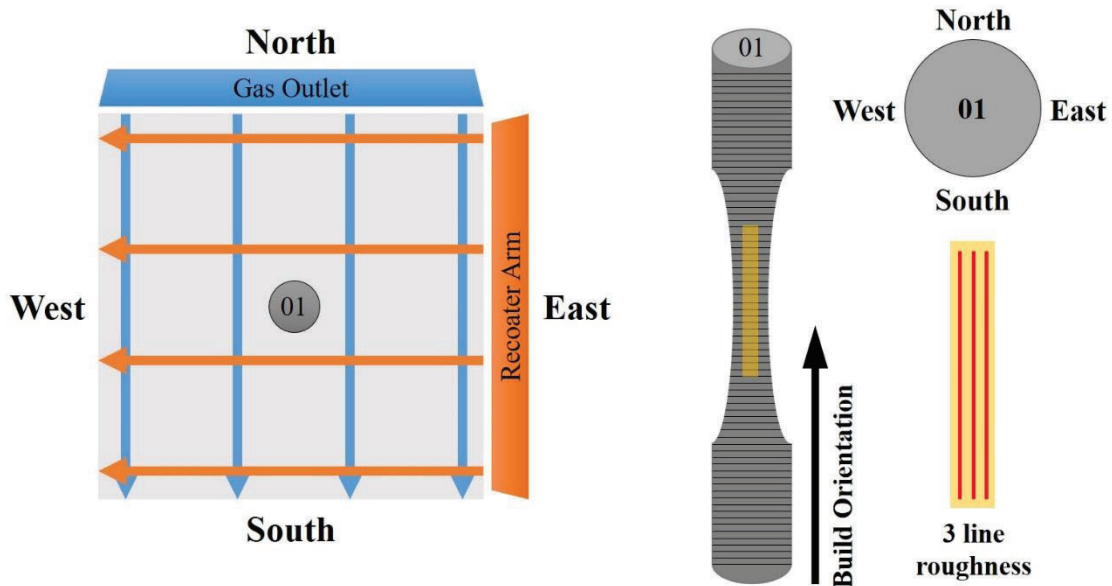


Figure 1. Schematic build orientation and profiled area for line roughness measurement.

Fatigue testing was conducted on an MTS Landmark (MTS, Minnesota, USA) servo-hydraulic test frame with a 100 kN capacity. A set of specimens were tested under force-controlled conditions with the remaining specimens being tested under strain-controlled conditions. For both loading conditions, an extensometer was attached on the side of the gage section to record the constitutive cyclic stress-strain relationship [14]. For strain-controlled fatigue testing, three different strain amplitudes of 0.002, 0.003, and 0.0075 (mm/mm) were conducted to incorporate high cycle fatigue (HCF), intermediate cycle fatigue (ICF), and low cycle fatigue (LCF) regimes.

For the force-controlled fatigue testing, the proper loading force was considered from the cross-sectional area and the desired stress amplitude.

Fractography for the cross-section of the fracture surface was also conducted using the Keyence VHX-6000. At first, the entire fracture surface was observed with low magnification to estimate overall fracture surface. The higher magnification images were captured to locate districts that contain crack initiation. Especially, for the as-built specimens, every crack initiated from the surface and therefore, the direction which has the highest surface roughness were more carefully studied.

### Results

Various representative parameters, which describe surface roughness with a numerical value such as (1) the arithmetic mean of all measured values on the profile ( $R_a$ ), (2) the maximum profile height ( $R_z$ ), and (3) the ten-point height of irregularities ( $R_z$ -ISO), were investigated by focal variation digital microscopy. In this study, arithmetical mean deviation ( $R_a$ ) represents the average surface roughness. The average of three measurements from the line-roughness profiles provided the final surface roughness values. This was carried out on each north, west, south, and east sides of the gage section with the resulting values shown in Table 1 with their standard deviations in parentheses. Box plots containing  $R_a$  values for all directions are shown in Figure 2 showing there is no significant difference in surface roughness for any face. Results show that on average the north face has the highest roughness while the south face has the lowest roughness. However, there is no tendency that the specific side has more surface roughness because each specimen shows different trends across each face.

**Table 1.** The average of three line roughness  $R_a(\mu\text{m})$  of specimens from each side.

Specimen ID	East	North	South	West	Average
09	11.53 (1.48)	10.84 (1.52)	11.34 (0.50)	10.29 (0.95)	11.00 (0.48)
14	12.15 (0.93)	11.49 (0.84)	13.82 (0.53)	10.77 (1.21)	12.06 (1.13)
15	11.21 (1.02)	10.42 (1.39)	12.48 (1.13)	10.86 (1.87)	11.24 (0.77)
21	10.74 (1.18)	11.35 (0.74)	9.18 (0.49)	8.64(0.91)	9.98 (1.10)
25	12.89 (1.31)	13.67 (0.79)	11.55 (1.08)	16.13 (1.54)	13.56 (1.67)
31	16.30 (1.08)	16.85 (1.96)	13.53 (1.39)	14.87 (1.84)	15.39 (1.29)
37	11.65 (0.60)	13.21 (1.46)	10.53 (0.77)	13.66 (1.28)	12.26 (1.25)
39	12.55 (0.78)	11.97 (1.32)	13.30 (2.45)	12.00 (1.66)	12.46 (0.54)
44	15.06 (0.72)	17.87 (2.04)	11.71 (0.93)	14.13 (0.51)	14.69 (2.21)
Average	12.68 (1.75)	13.07 (2.50)	11.94 (1.43)	12.37 (2.32)	12.51 (1.65)

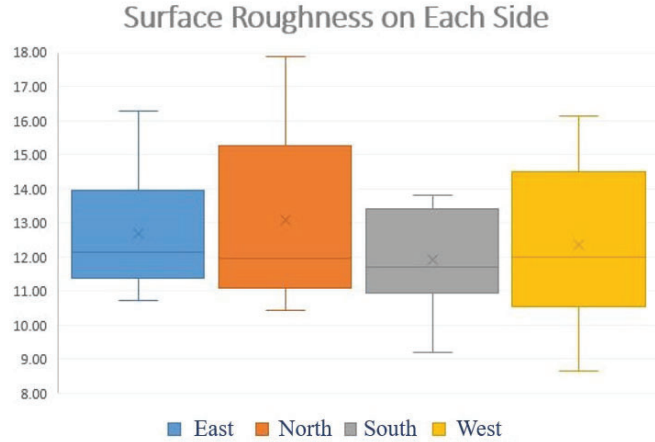


**Figure 2.** The box graph of surface roughness of each side for each specimen

**Figure 3** shows the strain amplitude versus reversal to failure (Strain-Life) graph in log-log scale. The results from the as-built condition specimens are shown as red squares and as-machined condition specimens are shown as blue diamonds. The strain-life curve consists of plastic and elastic regions, thus each plastic and elastic curves were calculated first and then combined to get the final strain-life curve. The final strain-life curves are displayed as dotted lines in **Figure 3**. **Table 2** lists the Manson-Coffin coefficients according to the condition of the surface. Manson-Coffin relationship explained as **Equation 1** below. The low cycle fatigue (LCF) behavior for both of as-built and as-machined condition were similar, however, the machined condition showed slightly better fatigue resistance. In the high cycle fatigue (HCF) regime, the machined condition showed even better fatigue resistance than the LCF. Even though this discrepancy is obvious in the HCF regime, the debit on the fatigue resistance is much smaller compared to most AM materials [4], [5] with only one order of magnitude difference in fatigue life.

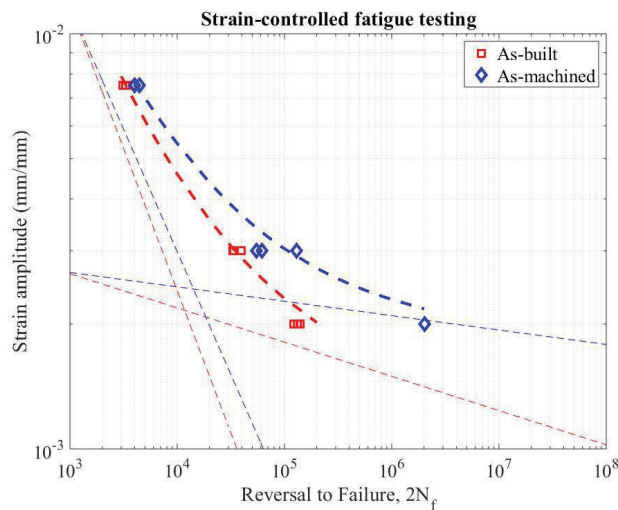


**Figure 3.** Strain amplitude (mm/mm) versus reversal to failure ( $2N_f$ ) graph of strain-controlled fatigue testing.

**Table 2.** Coefficients of strain-life curves according to the control mode of fatigue testing and condition of the surface.

	$\frac{\sigma_f'}{E}$	$b$	$\epsilon_f'$	$c$
Strain-controlled As-built	4.671E-03	-8.244E-02	1.322	-0.685
Strain-controlled As-machined	3.38E-03	-3.464E-02	0.688	-0.5907

**Equation 1.** Strain-life relationship

$$\frac{\Delta\epsilon}{2} = \epsilon_a = \frac{\Delta\epsilon_e}{2} + \frac{\Delta\epsilon_p}{2} = \frac{\sigma_f'}{E} (2N_f)^b + \epsilon_f' (2N_f)^c$$

Where,  $\frac{\Delta\epsilon}{2}$  = total strain amplitude =  $\epsilon_a$

$\frac{\Delta\epsilon_e}{2}$  = elastic strain amplitude =  $\frac{\Delta\sigma}{2E} = \frac{\sigma_a}{2E}$

$\frac{\Delta\epsilon_p}{2}$  = plastic strain amplitude =  $\frac{\Delta\epsilon}{2} - \frac{\Delta\epsilon_e}{2}$

$\sigma_f'$  and  $b$  = fatigue strength coefficient and exponent

$\epsilon_f'$  and  $a$  = fatigue ductility coefficient and exponent

**Equation 2.** Basquin equation

$$S_{N_f} = A(N_f)^B$$

Where,  $S_{N_f}$  = fully reversed fatigue strength at  $N_f$  cycles to failure

The results of fully reversed force-controlled fatigue testing with three different stress levels for both as-built and as-machined specimens are as shown in **Figure 4**. The two dotted lines represent as the Basquin curves. The coefficients of the blue dotted line are  $A = 980.8$  and  $B = -0.1048$  and red dotted line are  $A = 607.2$  and  $B = -3.852E-02$ . These are calculated by Matlab using Basquin equation as shown in Equation 2. Figure 4 reveals that, under force controlled conditions, the material is much more sensitive to surface roughness than when under strain-controlled conditions. For example, when the stress amplitude was 350MPa for the as-machined specimen,  $2N_f$  was already over 2,000,000 reversals while the as-built condition only reached 10,000 reversals, a difference of 2 orders of magnitude. Therefore, the range of stress amplitude for machined specimens was 350 MPa ~ 400 MPa and as-built specimens was 200 MPa ~ 375

MPa. In addition, there is a compelling distinction between the two surface conditions such as intersection (A) between two trend lines and slope (B).

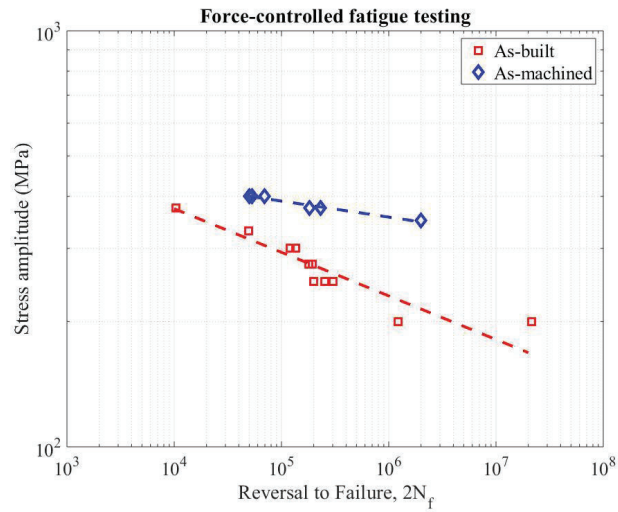


**Figure 4.** Stress amplitude (MPa) versus reversal to failure ( $2N_f$ ) graph of force-controlled fatigue testing.

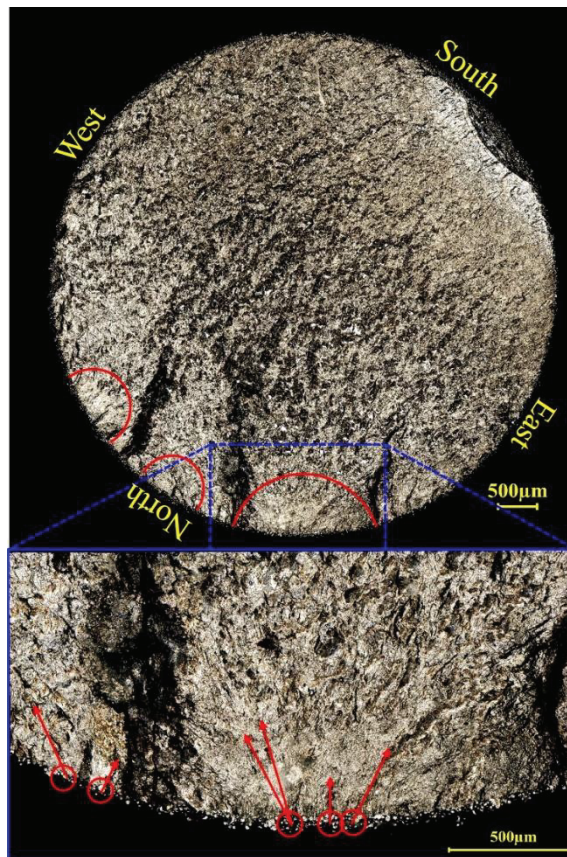


**Figure 5.** Fracture surfaces of strain-controlled tested as-built condition specimen #04. The strain amplitude was 0.002 (mm/mm) and the reversals to failure was 139,312.

The fractography analysis provides details regarding the fracture surface such as crack initiation and crack propagation. The observed fractographic image of specimen # 04, shown in **Figure 5**, details many of the common features observed for as-built specimens. This specimen was tested in the HCF regime at a strain amplitude of 0.002 (mm/mm). The fracture surface indicates that multiple cracks initiated on the north surface, coalesced into a single dominant crack, and grew through ~98.0% of the cross-sectional area before final rupture. **Figure 6** shows cross-sectional fracture surfaces two specimens tested under strain-control at  $\epsilon_a = 0.003$  (mm/mm) for (a) as-built condition specimen # 37 which has 47156 reversals to failure and (b) as-machined condition specimen # 18 which has 64080 reversals to failure. For the as-built condition, multiple cracks initiated from the southern side of specimen. On the other hand, the as-machined specimen had the dominant crack initiate on the surface, however, several cracks also initiated sub-surface.

**Figure 7** shows the fracture surfaces of two specimens tested under force-control at 375 MPa in the (a) as-built condition specimen # 13 and (b) as-machined condition specimen # 30. The crack initiation under force-controlled conditions show similar characteristics as strain-controlled fatigue such as multiple cracks initiating on the surface of the as-built condition and sub-surface cracks initiating on the as-machined condition. In addition, there is a striking difference in the crack growth behavior between strain-controlled fatigue as shown in **Figure 6** and force-controlled fatigue as shown in **Figure 7**. While the strain-controlled tests showed stable crack growth through the majority of the specimen cross-section, the force-controlled tests fail abruptly at approximately 40% of the cross-sectional area.

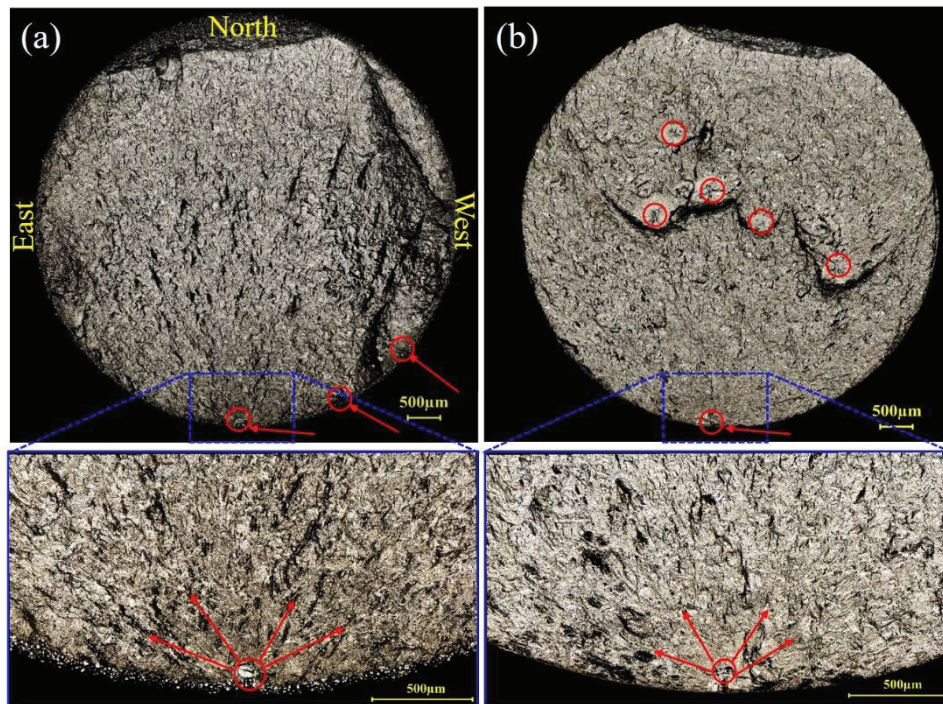


**Figure 6.** (a) Fracture surfaces of strain-controlled tested as-built condition specimen # 01. (b) Fracture surfaces of strain-controlled as-machined condition specimen # 18. For both specimens,

entire surface images were taken by 300X magnification and zoomed images were taken by 1000X magnification. Strain amplitude was 0.003 (mm/mm) for both of them.

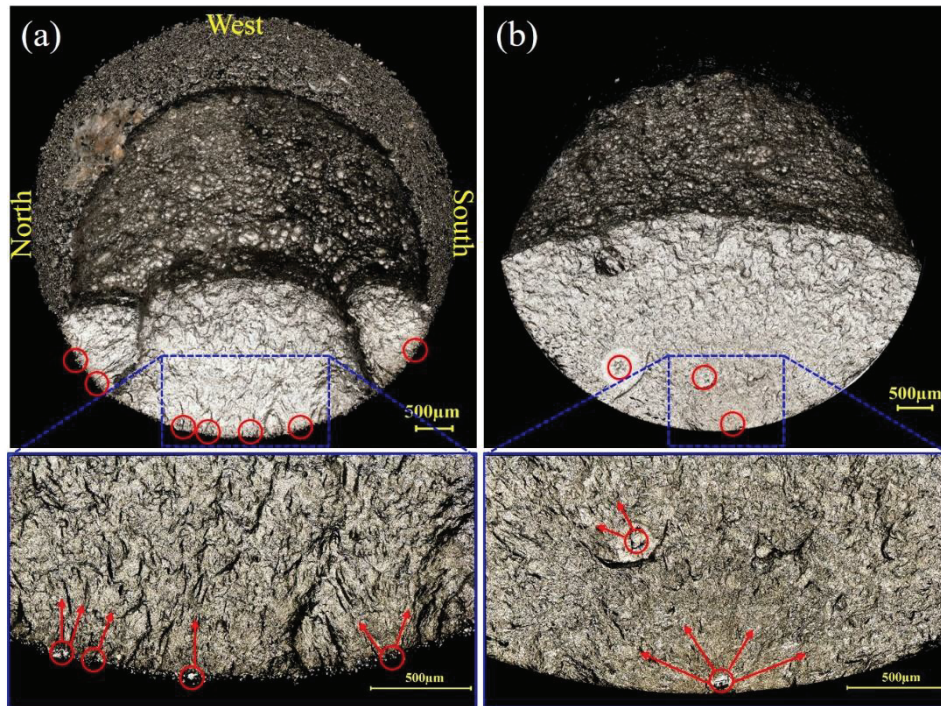


**Figure 7.** (a) Fracture surfaces of force-controlled tested as-built condition specimen # 13. (b) Fracture surfaces of force-controlled as-machined condition specimen # 30. For both specimens, entire surface images were taken by 300X magnification and zoomed images were taken by 1000X magnification. Stress amplitude was 375 MPa for both.

### Discussion

In this study, the tests in the as-built condition always showed cracks initiating from the rough surface, however, the actual crack initiation regions were often different from the highest surface roughness region. All of the crack initiation regions were investigated by fractography and compared with surface roughness data (Table 1). Arithmetical mean deviation ( $R_a$ ) can explain the surface roughness but it does not give the critical information needed to determine the crack initiation point. Maximum profile valley ( $R_v$ ) was also investigated as a different approach, but the results were also not sufficient to identify the critical location of the specimens. This is mostly due to the roughness values not capturing the geometry of the micro-notches. Previous studies on surface roughness effects of additive manufactured Ti-6Al-4V has shown that sufficient predictions can be made by incorporating a geometric term into the effective stress concentration factor estimation [15].

There are many factors that affect surface roughness such as the direction of a recoater arm, distribution of powder particle's size, and gas flow [16], [17], [18]. First, the powder was diffused by the recoater arm from the feedstock bin (east) to the overflow bin (west) between layers, hence

the height of each layer can be different because the blade on the recoater arm extrude the powder. Second, the variations in particle sizes can result in changes in the surface condition. If there is a large particle at the end of the part, this particle will remain as an un-melted powder on the surface because of the insufficient energy produced by laser process. This discrepancy is directly related to the distribution of powder. Third, the inert gas such as argon or nitrogen flow in the machine from north to south to decrease oxygen content during the printing. Some powder is ejected into the air when the laser interacts with the powder bed, at the same time the gas flow can carry these scattered powders which can disturb the powder bed near an unfused part or adhere them to a previously fused part. In the latter case the subsequent spreading of the powder can lead to an uneven layer of powder near the adhered particle and result in poor fusion at the surface or even within the part. In addition, the gas flow can become turbulent, especially at the corners of the plate resulting in the plume not being carried directly away from the laser beam path. When the plume interacts with the laser it can slightly defocus the laser leading to larger/smaller spot sizes and insufficient melting. This complicated gas flow gives rise to a higher probability of surface roughness variation as well as internal defects.

The main difference between fracture surfaces of as-built and as-machined specimens is the region of crack initiations. For as-built specimens under both strain-controlled and force-controlled fatigue, cracks are initiated from multiple places on the surface. They grow separately at the beginning, then coalesce leading to a single dominant crack. On the other hand, for as-machined specimens under both conditions, the main crack initiation point is at the surface and does not appear to be influenced by other cracks at the surface but does coalesce with cracks initiated from internal defects, as shown in **Figure 6 (b)** and **Figure 7 (b)**.

The specimens tested in force-control were revealed to be more sensitive to surface roughness than specimens tested in strain-control. For strain-controlled fatigue tests as shown in **Figure 6**, the crack growth is mostly similar between as-built and as-machined surface conditions. The cracks propagated up to 97.50% for (a) and 97.01% for (b). Under strain-controlled conditions the force to maintain the actual strain of the specimen reduces as the strain accumulates allowing the crack to remain stable throughout the entire fatigue life. On the other hand, for force-controlled fatigue tests as shown in **Figure 7**, the crack propagated to 30.36% for (a) and 45.30% for (b). The force-controlled fatigue testing maintains the force, thus increasing the actual stress as the crack develops and eventually leads to unbounded deformation. Thus, in the as-built condition this occurs suddenly as the multiple crack interact and coalesce leading to unstable crack growth. Conversely, under stain-control conditions the deformation in each cycle is limited by the loading condition and thus the crack grows at a stable rate regardless of its interaction with other cracks.

### **Conclusions**

The effects of surface roughness of the as-built condition of LB-PBF 304L SS AM under strain-controlled and force-controlled fatigue testing were investigated in this study. For

comparison, as-machined specimens were also fabricated and tested under the same conditions. As a result, four different fatigue life curves and the fractography images for each condition were obtained. The following conclusions can be made as a result of the findings:

1. Surface roughness can vary with no obvious correlation to direction. Even though the specimen has cylindrical design, surface roughness of each sides (north, west, south, and east) show variations.
2. The mechanical debit on fatigue life as-built and as-machined specimen under strain-control is much smaller than under force-control.
3. Multiple cracks initiated on the surface of the as-built specimens. However, there is only one crack initiation close to the surface of as-machined specimens.
4. Crack growth stability of force-controlled conditions is much lower for a propagating crack than strain-controlled conditions resulting in the observed discrepancy in fatigue resistance for the loading conditions.

#### **Acknowledgement**

This material is based upon work supported by the National Science Foundation (NSF) under Grant No. 1657195.

#### **References**

- [1] T. Wohlers and T. Gornet, "History of additive manufacturing Introduction of non-SL systems Introduction of low-cost 3D printers," *Wohlers Rep. 2016*, 2016.
- [2] S. M. Thompson, L. Bian, N. Shamsaei, and A. Yadollahi, "An overview of Direct Laser Deposition for additive manufacturing; Part I: Transport phenomena, modeling and diagnostics," *Additive Manufacturing*. 2015.
- [3] W. S. W. Harun, M. S. I. N. Kamariah, N. Muhamad, S. A. C. Ghani, F. Ahmad, and Z. Mohamed, "A review of powder additive manufacturing processes for metallic biomaterials," *Powder Technology*. 2018.
- [4] B. Bhushan and M. Caspers, "An overview of additive manufacturing (3D printing) for microfabrication," *Microsyst. Technol.*, 2017.
- [5] J. Pegues, M. Roach, R. Scott Williamson, and N. Shamsaei, "Surface roughness effects on the fatigue strength of additively manufactured Ti-6Al-4V," *Int. J. Fatigue*, 2018.
- [6] L. Huynh, J. Rotella, and M. D. Sangid, "Fatigue behavior of IN718 microtrusses produced via additive manufacturing," *Mater. Des.*, 2016.
- [7] W. E. Frazier, "Metal additive manufacturing: A review," *Journal of Materials Engineering and Performance*. 2014.
- [8] J. Boér and P. Blaga, "Reducing production costs by monitoring the roughness of raw product surfaces," in *Procedia Manufacturing*, 2018.
- [9] R. R. I. Stephens, A. Fatemi, R. R. I. Stephens, and H. O. Fuchs, *Metal Fatigue in Engineering*. 2000.

- [10] S. Leuders *et al.*, “On the mechanical behaviour of titanium alloy TiAl6V4 manufactured by selective laser melting: Fatigue resistance and crack growth performance,” *Int. J. Fatigue*, 2013.
- [11] P. E. Carrion, A. Soltani-Tehrani, N. Phan, and N. Shamsaei, “Powder Recycling Effects on the Tensile and Fatigue Behavior of Additively Manufactured Ti-6Al-4V Parts,” *JOM*, 2019.
- [12] A. Fatemi, R. Molaei, S. Sharifimehr, N. Shamsaei, and N. Phan, “Torsional fatigue behavior of wrought and additive manufactured Ti-6Al-4V by powder bed fusion including surface finish effect,” *Int. J. Fatigue*, 2017.
- [13] ASTM E606/E606M, “Standard Test Method for Strain-Controlled Fatigue Testing,” *ASTM Standards*. 2012.
- [14] E1492-98(2004), “Standard Guide for Evaluating Data Acquisition Systems Used in Cyclic Fatigue and Fracture Mechanics Testing,” in *ASTM Book of Standards*, 2000.
- [15] J. W. Pegues, N. Shamsaei, M. D. Roach, and R. S. Williamson, “Fatigue life estimation of additive manufactured parts in the as-built surface condition,” *Mater. Des. Process. Commun.*, 2019.
- [16] E. Wycisk, A. Solbach, S. Siddique, D. Herzog, F. Walther, and C. Emmelmann, “Effects of defects in laser additive manufactured Ti-6Al-4V on fatigue properties,” in *Physics Procedia*, 2014.
- [17] Y. M. Arisoy, L. E. Criales, T. Özel, B. Lane, S. Moylan, and A. Donmez, “Influence of scan strategy and process parameters on microstructure and its optimization in additively manufactured nickel alloy 625 via laser powder bed fusion,” *Int. J. Adv. Manuf. Technol.*, 2017.
- [18] P. Bidare, I. Bitharas, R. M. Ward, M. M. Attallah, and A. J. Moore, “Fluid and particle dynamics in laser powder bed fusion,” *Acta Mater.*, 2018.